A sub-grid scale cavitation inception model

Mehedi H. Bappy[1], Pablo M. Carrica[1,*], Jiajia Li[1], J. Ezequiel Martin[1], Alberto Vela-Martin[2], Livia S. Freire[3], Gustavo C. Buscaglia[3]

[1]IIHR-Hydrscience and Engineering, The University of Iowa, Iowa City, Iowa 52242, USA
[2]ETSIAE, Universidad Politécnica de Madrid, Madrid 28040, Spain
[3]Instituto de Ciências Matemáticas e de Computação, Universidade de São Paulo, São Carlos, Brazil
[*]Corresponding author, pablo-carrica@uiowa.edu

Abstract

Unresolved pressure fluctuations at the subgrid scale (SGS) level of Large Eddy Simulation (LES) or Reynolds-averaged Navier-Stokes (RANS) computations affect cavitation inception predictions, as SGS low pressures are simply ignored. We present a framework to take the unresolved SGS flow into account. Representing the SGS flow as canonical turbulence, in this paper homogeneous isotropic turbulence (HIT), the pressure fluctuations, transport and cavitating behavior of nuclei in such turbulence can be evaluated from direct numerical simulations (DNS) and used to create a model of cavitation inception that accounts for SGS fluctuations. To accomplish this, nuclei of different sizes were transported in DNS of HIT, using their pressure history to drive the Rayleigh-Plesset equation that simulates bubble dynamics. In this way, expected average cavitation frequencies were tabulated for a range of SGS Taylor scale Reynolds numbers (Re_λ), nuclei size, TKE dissipation rate, and mean pressure. The model uses this table to estimate the cavitation event rate in each cell of a computational fluid dynamics (CFD) solution. Inception can then be predicted by comparing the total cavitation rate with the detection criterion. The model is first assessed on two cases of HIT (at Re_λ=240 and 324) by comparing the pressure statistics it predicts in LES runs using the SGS cavitation model against the statistics of DNS. Then, a high Re_λ (1660-1880) HIT flow is simulated using LES and cavitation events are compared against experimental data. The inception model successfully predicts the inception pressure and the cavitation rates in the flow.

1. Introduction

Cavitation in liquids occurs when pressure in the flow falls below vapor pressure and results in fluid evaporation. Cavitation creates vapor bubbles that grow and then collapse as the pressure recovers above vapor pressure, sometimes causing intense shock waves. While most common in turbomachinery (pumps, turbines, marine propellers), it also occurs in pipes and valves, control surfaces in high-speed marine craft, concrete and rocks in high-speed streams and spillways, and a variety of other natural and man-made systems. Some undesired effects of cavitation are noise, erosion and loss of performance in turbomachinery. Cavitation must be prevented for many applications, and thus prediction of conditions for cavitation inception is critical. Besides experiments, computational fluid dynamics (CFD) can be used to analyze cavitation inception problems.

Pressure fluctuations are key to the phenomenon of cavitation inception in turbulent liquid flows, where microscopic bubbles (or nuclei) present in the liquid grow to produce detectable vapor bubbles (Brennen 1995, Mørch 2015). The evolution of isolated nuclei undergoing a pressure history can be simulated using the Rayleigh-Plesset equation (Brennen 1999 and references therein), but proper prediction of cavitation inception in practical flows remains a challenge (Arndt 2002, Li 2015, Li et al. 2015), mostly due to the inability of predicting the pressure histories experienced by nuclei in the fluid, as the relevant low-pressure structures responsible for cavitation inception are very small and might not be resolved when using standard CFD approaches with current computer resources.

Direct numerical simulation (DNS) of the liquid/gas coupled flow, including appropriate physical modeling of the flow and thermodynamics of nuclei and cavitating vapor bubbles, see for instance Okabayashi and Kajishima (2011), would be capable of solving the problem as no turbulence model is involved and all scale and physical processes would be resolved. This approach is severely limited by the spatial and temporal resolution necessary to handle the small sizes and fast transients occurring during cavitation, typically considerably more demanding than the requirements to resolve turbulence, making it impractical except for the simplest geometries and a few bubbles.

Less demanding than full DNS, but still beyond current computational capabilities, is a one-way coupled approach in which the liquid flow is computed with DNS ignoring the presence of nuclei and incipient vapor bubbles. This methodology requires a model to predict the inception of cavitation by solving the dynamics of the nuclei as they grow and cavitate in presence of low pressures, for instance solving the Rayleigh-Plesset equation (Brennen 1995) along the bubbles' trajectories. A one-way coupling approach is appropriate if the gas volume fraction is low enough and thus does not influence the liquid flow. As a reference example, the void fraction produced by a relatively high concentration of 10 nuclei/cm^3 of 50 micron diameter nuclei is 6.5×10^{-7}. In practice the nuclei concentration is typically limited to the range 0.1~10 nuclei/cm^3. Since before inception the void fraction caused by the nuclei and incipient cavitation is very low, it is safe to assume that the bubble dynamics will not significantly affect the liquid pressure and velocity distribution.

Cavitation inception is determined experimentally using either visual or acoustic detection methods. In visual methods, the inception of cavitation is determined by observing the flow for initiation of vapor cavities (Hsiao et al. 2003, Straka et al. 2010). This method has uncertainties caused by the need for illumination, sensitivity to the viewer, and the size of the cavities. Acoustic methods analyze the acoustic signal of the cavitation noise looking for pops and later chirps as the reference pressure is decreased (Song 2017); acoustic methods are sensitive to background noise and detection threshold. It should be noted that there are no absolute visual/acoustic detection criteria (size or noise and frequency levels) which adds uncertainty to the prediction of cavitation inception.

In case of numerical simulations, three types of inception criteria and techniques are most common. The simplest is to perform a liquid flow simulation and use the minimum pressure to determine the cavitation inception index. Wimshurst et al (2018) used the minimum resolved pressure criteria to detect cavitation inception on flow around turbine blades at different tip-speed ratio and submersion depth. Asnaghi et al. (2018) proposed an alternative method based on the energy of low pressure region where they estimate the diffused vapor volume due to pressure going below the vapor pressure to identify the inception points. A second approach is to simulate both liquid and vapor phases in an Eulerian fashion. Cavitation inception is determined when vapor cavites reach a volume of detectable size (Asnaghi et al. 2018, Brandao and Mahesh 2022). Brandao and Mahesh (2022) simulated cavitation in a shear layer behind a backward facing step using a one-way coupling approach, and counted the frequency of cavitation events to determine the onset of cavitation. The one-way coupling allows solving the vapor transport equation as in a homogeneous mixture model, enabling variation of the cavitation number without the need to recompute the liquid flow. The low void fractions involved justify the one-way approach, as done in this paper.

A third type of analysis is an Eulerian-Lagrangian approach where a resolved pressure field is used to compute the bubble dynamics. Several early attempts to compute cavitation inception have combined RANS and LES approaches with the solution of the dynamics of transported nuclei (Kodama et al. 1981, Meyer et al. 1992, Hsiao and Pauley 1999, Hsiao and Chahine 2004), using the resolved pressure to solve a Rayleigh-Plesset equation. Usually a spatially limited grid of higher resolution is used to capture the small scale fluctuations where cavitation is expected (Hsiao and Chahine 2004). One advantage of this technique is that it can more easily account for the effects of water quality. The influence of water quality on cavitation inception prediction was investigated by Chen et al. (2019) in the context of tip vortex cavitation. They used several nuclei concentrations and size distributions while they released the from different distances from the core of the vortex. With the resulting bubble dynamics, they formulated an analytical relation for capture time. Their analysis show that the inception index can change up to 10% based on the nuclei distribution. The effect of non-condensable gases (NCG) for tip vortex cavitation has recently been studied by Cheng et al. (2021). They proposed a new model accounting for the NCG using a Euler-Lagrangian cavitation model and showed the important role of the gas content in sustaining cavitation.

In any CFD methodology other than DNS, a SGS turbulence model is used to obtain proper solutions of the resolved flow. The SGS flow is filtered out and thus pressure fluctuations at the SGS level are not part of the resolved flow. Consequently, low pressures occurring at the SGS level are ignored in any model attempting to predict cavitation inception directly from Large Eddy Simulation (LES) or Reynolds-averaged Navier-Stokes (RANS) pressure solutions. While still expensive, large eddy simulation (LES) can be used to tackle a wide variety of engineering problems and is attractive because many important characteristics of the flow are retained by resolving the largest turbulence scales. RANS is a mature modeling approach that can today be considered of low cost, while hybrid RANS/LES approaches like DES (Spalart 2009) are somewhere between RANS and LES in terms of cost and ability to resolve flow transients.

The need to account for unresolved pressure fluctuations in cavitation models has been recognized by Singhal et al. (2002), who added a simple correction to the resolved pressure based on the modeled turbulent kinetic energy (TKE) k as $P_v = P_{vap} + 0.195\rho k$, where P_{vap} is the vapor pressure under local conditions and P_v is the corrected vapor pressure, which by virtue of being higher than the local vapor pressure results in earlier cavitation inception. Anton (1993) analyzed the effects of turbulent stresses on inception, proposing a correction related to the Reynolds stresses. Joseph (1998) proposed a cavitation inception criterion of maximum tension trying to unify the theory of cavitation, the theory of maximum tensile strength of liquid filaments, and the theory of fracture of amorphous solids. This criterion has been used successfully with a Lattice Boltzmann CFD approach to compute inception (Ezzatneshan 2017), showing the potential to obtain higher cavitation inception numbers than using the pressure alone to drive cavitation, but has not been explored in this paper.

In this paper we present a cavitation inception modeling approach that accounts for unresolved SGS pressure fluctuations, building on previous work from the authors studying pressure statistics in turbulent flow in the context of cavitation inception (Bappy et al. 2019a, 2019b, 1020a, 2020b). The work on SGS cavitation inception is scarce, and most studies still use the resolved pressure to predict cavitation inception or to activate evaporation or condensation in cavitation models. With RANS, LES and hybrid RANS/LES approaches in mind, it is of interest to develop an SGS model for cavitation inception that can account for the unresolved pressure fluctuations. Okabayishi and Kajishima (2011) employed a probability density function (pdf) based SGS model to improve cavitation inception prediction with LES. Their model assumed a gaussian pressure distribution in the SGS and did not have any Lagrangian bubble dynamics component. Our model at this time uses statistics built from DNS simulations of HIT flow to compute SGS cavitation rates, though the model can easily be extended to more complex but appropriate canonical SGS turbulent flows, like homogeneous shear turbulence (HST), as discussed later. Details of the DNS simulations, Lagrangian nuclei transport for each size, cavitation rate computation from the Rayleigh-Plesset equation, final implementation of the model, and application to cavitation inception in HIT at high Reynolds numbers are discussed in the next sections.

2. Methodology

2.1 Sub-grid scale flow

In LES, pressure fluctuations at the SGS flow are not resolved. To incorporate the effects of those lost pressure fluctuations on the cavitation inception process, we use statistical information obtained by transporting millions of finite nuclei in DNS fields of homogeneous isotropic turbulence. Using HIT is convenient, as it is the simplest form of turbulent flow. If the LES simulations can resolve small enough scales, the SGS flow will be independent of the large scale flow and its scale statistics should be universal as postulated by Kolmogorov (1962) and later discussed in the context of homogeneous isotropic turbulence (Van Atta 1991) and homogeneous shear turbulence (Pumir 1996). Notice that HIT flows depend on a single parameter, the Reynolds number based on the Taylor microscale λ

$$Re_\lambda = \frac{u'\lambda}{\nu} \tag{1}$$

where u' is the RMS of the unresolved SGS turbulent velocity fluctuations and $\lambda = u'\sqrt{15\nu/\varepsilon}$ with ε and ν being the TKE dissipation and kinematic viscosity, respectively. In a LES field, the sub-grid velocity fluctuations u', and the sub-grid dissipation ε, and thus Re_λ varies from grid point to grid point. The sub-grid pressure fluctuations at each grid point are modeled as those experienced by nuclei immersed in a HIT flow corresponding to the local Re_λ. To compute quantitative estimates of cavitation rates from this model assumption, a database is built containing pressure histories of nuclei of different sizes tracked along DNS fields of several Re_λ: 22, 35, 55, 90, 150 and 240. The DNS solver, the tracking algorithm, and the treatment of the pressure histories to arrive at a sub-grid cavitation rate are detailed in the next sections.

2.1.1 Homogeneous isotropic turbulence solver

We performed simulations of a forced homogeneous and isotropic turbulent flow contained in a triply periodic cubic box, of size *N* in each direction. The flow is described by the Navier-Stokes equations,

$$\partial_t u_i + u_j \partial_j u_i = -\partial_i p + \partial_j \tau_{ij} + q_i, \tag{2}$$

$$\partial_i u_i = 0, \tag{3}$$

where u_i is the velocity vector, ρ is the density of the fluid, and p is the pressure that ensures the incompressibility of the flow, $\partial_i u_i = 0$, q_i is a body force that sustains turbulence. τ_{ij} represents the viscous stresses and is given by

$$\tau_{ij} = 2\nu S_{ij}, \tag{4}$$

where $S_{ij} = 1/2(\partial_i u_j + \partial_j u_i)$ is the rate of strain tensor and ν is the kinematic viscosity. The evolution equations are projected on a Fourier basis with $N/2$ modes in each direction and the non-linear terms are calculated using a pseudo-spectral method (Cardesa et al. 2017). The time-integration is performed using a third-order semi-implicit Runge-Kutta. The forcing term injects a

fixed amount of energy per unit time and is applied only to modes with $k < 2$, where k is the wavenumber magnitude in Fourier space.

Note that ν is adjusted to maintain a fixed numerical resolution $r = k_{max}\eta$. Here, η is the Kolmogorov length scale and $k_{max} = \sqrt{2}N/3$ is the maximum wavenumber magnitude. The Kolmogorov length scale is computed as

$$\eta = (\nu^3/\varepsilon)^{1/4}, \tag{5}$$

For a fixed resolution, and imposing a dimensionless dissipation level of $\varepsilon = 1$, the kinematic viscosity is

$$\nu = (r/k_{max})^{4/3}. \tag{6}$$

2.1.2 Eulerian and Lagrangian pressure statistics in HIT for finite nuclei

Eulerian pressure statistics in HIT have been studied by several authors (Pumir 1994, Cao et al. 1999, Gotoh and Rogallo 1999, Bappy et al. 2019b, 2020b). Time histories of the minimum pressure in the computational domain show that as Re_λ increases the absolute value of the minimum pressure and the amplitude of the pressure fluctuations increase, see Fig. 1.

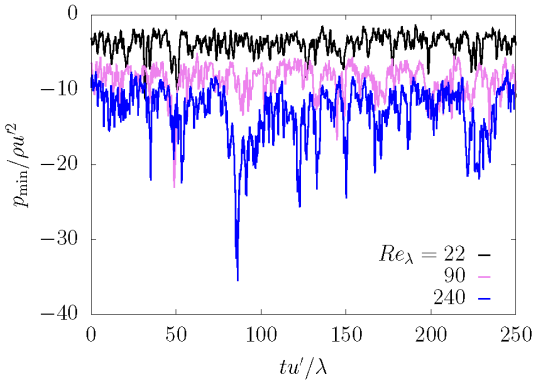

Figure 1: Normalized history of minimum pressure for $Re_\lambda = 22, 90$ and 240. The Kolmogorov timescale is 0.2582 for all Reynolds numbers and the integral timescales are respectively 1.4, 2.7, and 6.4 for $Re_\lambda = 22, 90$ and 240. The grid size N for DNS are 128, 256, and 512 with corresponding numerical resolution $r = 7.6, 3$, and 1.5 respectively for $Re_\lambda = 22, 90$ and 240.

The pdf of pressure is negatively skewed with an exponential tail at very low pressures, as shown by Cao et al. (1999) for Re_λ up to 148 and by Bappy et al. (2019b) for $Re_\lambda = 150$ and 418. Figure 2 shows the pdf of pressure for the range of Re_λ used in this paper for statistically stationary HIT. In these pdfs two clear trends of interest are observed: 1) as seen in Fig. 1, lower pressure can be achieved as Re_λ increases, and 2) the probability of reaching a given low pressure increases

as Re_λ increases. It appears that this trend saturates beyond $Re_\lambda = 150$, though this trend cannot be confirmed as only one higher Re_λ is available.

In the context of cavitation inception, the relevance of Lagrangian pressure statistics instead of Eulerian statistics has been discussed by several authors (Arndt and George 1979, La Porta et al. 2000, Bappy et al. 2019b). While small nuclei behave as tracers and thus experience pressures with Eulerian pdfs as the fluid particles do, larger nuclei are attracted to low pressure vortex cores and their Lagrangian pressure histories are pertinent (Bappy et al. 2019b, 2020b). Higher concentration of nuclei in low pressure regions result in higher probability of inception. We use nuclei of different sizes to obtain their appropriate cavitation inception statistics in the turbulent flow field, thus accounting for the nuclei size distribution in the water.

In our computation, the trajectories of the nuclei in the turbulence field are determined by integrating the transport equation coupled with a modified Maxey-Riley equation, namely

$$\frac{d\boldsymbol{x}(t)}{dt} = \boldsymbol{v}(t) \tag{7}$$

$$\frac{d\boldsymbol{v}}{dt} = \frac{1}{\tau_{\text{part}}}(\boldsymbol{u} - \boldsymbol{v}) + 3\boldsymbol{a}. \tag{8}$$

Here, $\boldsymbol{x}(t)$ and $\boldsymbol{v}(t)$ are the position and velocity of a nucleus at time t, respectively, and d/dt represents the time derivative along the particle trajectory. $\boldsymbol{u}$ and $\boldsymbol{a}$ are the fluid velocity and acceleration at the particle position and at time t. The non-dimensional inertial time of the nucleus is τ_{part} and is derived from Stokes' law. It relates to the turbulence intensity and nucleus size by

$$\tau_{\text{part}} = \frac{Re_\lambda}{9} {R_0}^{*2}, \tag{9}$$

where the dimensionless radius for a nucleus of equilibrium radius R_0 at the local pressure is defined as

$${R_0}^* = \frac{R_0}{\lambda}. \tag{10}$$

The pressure history is saved following all the nuclei along their trajectories and statistics are computed afterwards. The numerical algorithm for nuclei tracking is explained in more detail in Bappy et al. (2020b).

Probability density functions of the pressure experienced by nuclei with ${R_0}^* = 0.1$ are shown in Fig. 3. Comparing to Fig. 2, the probability of experiencing low pressures increases by up to two orders of magnitude, with stronger effect at lower pressures and higher Re_λ. Previous studies of light particles in turbulent flow show that the size of the particle has a considerable effect on its response to pressure fluctuations (Toschi and Bodenschatz 2009, Balachandar and Eaton 2010). The study of the effects of nuclei size and gravity on similar pressure statistics confirms

that larger nuclei experience more frequent pressure fluctuations and spend longer time in low pressure regions of the flow. Physically, larger nuclei experience more attraction towards low pressure vortex cores as both pressure gradient and drag forces increase with the cross sectional area, but the drag coefficient decreases with increasing size. Once the nuclei are positioned inside the core, they get trapped until the vortex dissipates. As the strength of the vortices increases for higher Re_λ so does the effect on pressure statistics. The response of the nuclei, as seen from the pressure pdfs, is significantly more favorable for cavitation. Such response as a function of nuclei size is documented by Wang (1999) and Bappy et al. (2020a, 2020b). Note that the limiting behavior observed for Eulerian statistics is no longer present at low pressure values and the probability of a nuclei experiencing a given low pressure continues to increase with Re_λ.

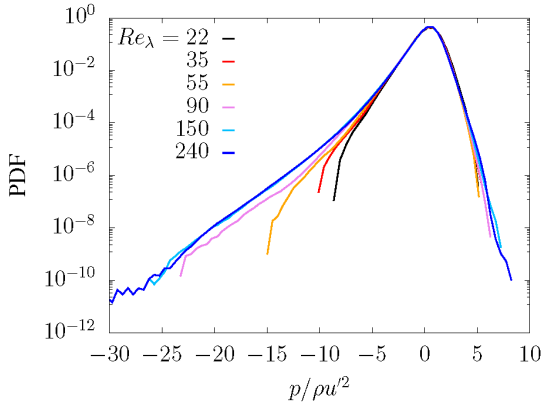

Figure 2: Probability density functions of Eulerian pressure at different Re_λ.

Of critical importance for cavitation are the frequency and duration of the low-pressure events experienced by the nuclei. The frequency of such events along with their duration determines the frequency of cavitation events in the flow, as discussed by several authors (Arndt and George 1979, La Porta et al. 2000). In the context of HIT, their dependence on pressure levels and Reynolds number has been explored by Bappy et al. (2019b, 2020b). The average low pressure event frequency (ζ) is defined as the number of low pressure excursions with pressure dropping below a certain level and recovering above the same level per unit time per particle. The average time required for each excursion is the average duration (d) of the low pressure event. The frequency of low-pressure events of any duration exponentially decreases as the pressure decreases, and similarly follows an exponential reduction for any level of pressure as the duration increases. The size of the nuclei affects the frequency significantly; a five-fold increase in size can result in an increase of several orders of magnitude in frequency of low-pressure events. This increase in frequency is more intense at lower pressures and thus can impact the cavitation more

significantly. Higher levels of turbulence in the flow are associated with more intense vortical structures, resulting in more frequent low-pressure events as Re_λ increases. This has been verified in this study for $22 \leq Re_\lambda \leq 240$. Figure 4 shows the frequency distribution of nuclei of sizes ${R_0}^* = 0.05$ and 0.10 at $Re_\lambda = 35, 90,$ and 240. It is evident that larger nuclei experience more frequent low-pressure events at all Re_λ and higher Re_λ exhibits higher frequency at low pressure levels.

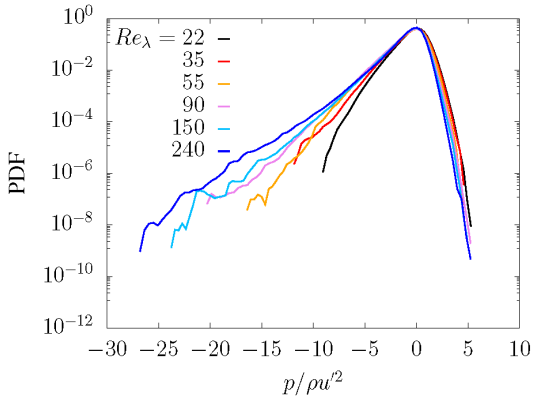

Figure 3: Probability density functions of pressure for nuclei of size $R_0^* = 0.1$ at several Re_λ. The limited number of events at very low pressure causes the rough tails.

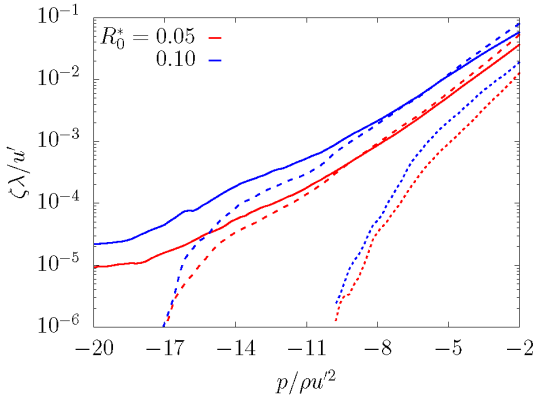

Figure 4: Low pressure event frequency distribution ζ for ${R_0}^* = 0.05$ and 0.10 for $Re_\lambda = 35$ (dotted), 90 (dashed), and 240 (solid).

While larger nuclei have a higher probability of experiencing and staying longer at extreme low pressures (Bappy et al. 2020b), the average duration as a function of nuclei size shows non-monotonic behavior. Figure 5 shows that all the curves behave similarly, initially increasing the average low pressure event duration with nuclei size and then gradually decreasing for $R_0{}^* > 0.05$. In general, higher Re_λ results in an increase of the average duration of the low-pressure events, though for larger nuclei and lower pressures differences become negligible. The combined effect of Re_λ and $R_0{}^*$ on the cavitation rate is discussed in §2.1.3.

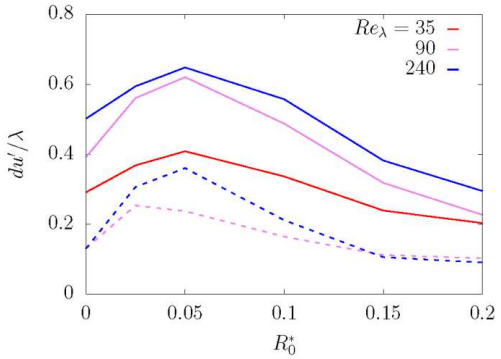

Figure 5: Average duration d of low-pressure events for $\frac{p}{\rho u'^2} = -7.5$ (solid) and -15.0 (dashed) for three Re_λ. There is no curve for $\frac{p}{\rho u'^2} = -15.0$ and $Re_\lambda = 35$ since fluctuations for this case do not reach such low pressure, see Fig. 2. Average duration increases with nuclei size up to $R_0{}^* > 0.05$, then gradually decreases.

2.1.3 Cavitation rate on HIT

In turbulent flows, intense fluctuations of pressure below the cavitation pressure can cause gas nuclei to undergo exponential growth and a subsequent collapse when the pressure rises again above cavitation pressure. The dynamics of spherical bubbles in a pressure field can be estimated by the Rayleigh-Plesset (RP) equation (Brennen 1995). To model the equivalent cavitation rate at the subgrid scale in LES, the time histories of pressure obtained from transport of nuclei in DNS solutions are used to solve the evolution of the nuclei radius. For a nucleus exposed to a pressure history $P(t)$ the evolution of the radius $R(t)$ is obtained from

$$\rho_L\left(\frac{3}{2}\dot{R}^2 + R\ddot{R}\right) + \frac{4\mu\dot{R}}{R} = p_{vap} + \left(p_{atm} + \frac{2S}{R_{atm}} - p_{vap}\right)\left(\frac{R_{atm}}{R}\right)^{3\gamma} - \frac{2S}{R} - P(t) \qquad (11)$$

In Eq. (11), $\dot{R} = \frac{dR}{dt}$, $\ddot{R} = \frac{d^2R}{dt^2}$, ρ_L and μ are the liquid density and viscosity, respectively, p_{vap} is the vapor pressure of the liquid, S is the surface tension, and γ is the polytropic exponent of the non-condensable gas. R_{atm} is the radius of the nucleus in equilibrium at rest at a uniform temperature T_{atm} and pressure p_{atm}. Effects of temperature on all physical properties are neglected. If the pressure fluctuations are $P'(t)$, a nucleus will go through a time varying pressure field given by

$$P(t) = P_0 + P'(t). \tag{12}$$

This pressure history is obtained for Lagrangian nuclei transported in the HIT field as previously described, with R_0 taken as the equilibrium radius at pressure P_0. Of course, the value of $R_0^* = R_0$ must coincide with the one used in the computation of the pressure history $P'(t)$. The summation of the right-hand side terms of Eq. (11), except $P(t)$, denoted as $F_{NN}(R)$, takes a minimum value for any $R(t) > 0$. The radius R_* where $F_{NN}(R)$ is minimum is the Blake critical radius and $F_{NN}(R_*) = \min(F_{NN})$ can be defined as the cavitation pressure or Blake's critical pressure, p_{cav}.

$$p_{cav} = \min\left(F_{NN}(R)\right)_{R>0} = F_{NN}(R_*)$$
$$= p_{vap} - \frac{3\gamma-1}{3\gamma}\left[\frac{(2S)^{3\gamma}}{3\gamma\left(p_{atm}+\frac{2S}{R_{atm}}-p_{vap}\right)R_{atm}^{3\gamma}}\right]^{1/(3\gamma-1)}. \tag{13}$$

If $P(t) < p_{cav}$ and $P(t) = constant$, the initially small sized bubble rapidly grows and cavitates reaching a detectable size. For any temporally evolving functions $P(t)$ that plummet below p_{cav} for a limited time, it is not obvious whether the bubble will grow to detectable sizes or not, therefore it is necessary to solve the RP equation along the nuclei trajectory and establish a detection criterion for cavitation.

The criterion for cavitation inception can be based on either visual or acoustic detection limit. For visual cavitation, when a bubble grows beyond a limiting detectable value is considered a cavitation event (Hsiao et al. 2003, Straka et al. 2010). For acoustic detection, when the acoustic pressure emitted by a growing/collapsing bubble exceeds a limiting threshold then a cavitation event is counted (Ran & Katz 1994, Song 2017). This criterion is very important and will change the cavitation event rates directly. With a smaller observable (e.g., 500 microns, probably the smallest bubbles observable with the bare eye, though video can these days observe much smaller cavities), we will have a higher cavitation event frequency and with a larger criterion (e.g., 1000 microns), we will have a lower frequency. In this study, we used a nuclei cavitation criterion of $R \geq 500$ microns based on the ability to visually detect the growing bubbles.

The average cavitation rate f_{cav} [events/particle/s] was computed as

$$f_{cav} = \frac{N_{cav}}{M(\lambda\tilde{T}/u\prime)}, \tag{14}$$

where N_{cav} is the number of cavitation events tallied from the bubble dynamics simulation, M is the total number of particles seeded in HIT domain, and $\tilde{T}$ is the total nondimensional time of the

DNS HIT simulation. Cavitation event rates are computed for a cavitation event criterion of $R = 500$ μm as previously discussed. The method of computing the cavitation event rates from the RP solutions is the same as discussed in Bappy et al. (2020b), however, in that paper two cavitation inception criteria were used based on the size of the bubble: $R = 250$ microns, and $R = 10R_0$.

The numerical procedure adopted to integrate the RP equation along the nuclei trajectory is a fourth order embedded Runge–Kutta method with an adaptive time step applied to a scaled version of the equation to reduce round-off errors. The initial conditions to start the integration are $\dot{R}(0) = 0$ and $R(0)$ such that $F_{NN}(R(0)) = P(0)$. Note that $P(0)$ varies from bubble to bubble and, in general, is different from the average pressure P_0 of the liquid. The dimensionless fluctuating pressure history $P'_{HIT}(t)$ of a Lagrangian particle from HIT is transformed to a dimensional history by

$$P'(t) = P'_{HIT}\left(t\frac{u'}{\lambda}\right) \times \rho_L u'^2. \tag{15}$$

The subscript HIT denotes trajectories from Lagrangian particles seeded in the HIT flow and $t\frac{u'}{\lambda}$ is the nondimensional time of HIT flow. Both R_{atm} and P_0 are varied to simulate bubbles of different sizes in HIT with different mean pressures. The material parameters were given fixed values representative of water under ambient conditions: $\rho_L = 1000$ kg/m3, $\mu = 10^{-3}$ Pa s, $S = 0.07$ Pa m, $\gamma = 1.4$, and $p_{vap} = 2340$ Pa. In addition, nuclei are treated separately and independently. It is conceivable that a cavitating bubble may locally alter the pressure field to influence the inception in a nearby nucleus, and either induce or inhibit inception. This coupling between nuclei has also been neglected, as nuclei are separated in average by about 100 times the nuclei diameter for the void fraction discussed above.

The cavitation event rates depend not only on R_{atm} and P_0 but also on the SGS Taylor scale Reynolds number (Re_λ), and on the turbulent kinetic energy dissipation rate (ε), as discussed later in §2.2.1. Table 1 shows the range of parameters adopted for solving the RP equation and build the database. Note that the total number of nuclei seeded into the HIT domain for solving RP is 32^3 for $Re_\lambda = 22 - 150$ and 50^3 for $Re_\lambda = 240$. The total integral time used for these simulations are approximately 376, 530, 760, 555, 820, and 571 for $Re_\lambda = 22, 35, 55, 90, 150,$ and 240 respectively.

Figure 6 presents the cavitation event rate f_{cav} as a function of P_0 and R_0 for different values of the other model inputs Re_λ and ε due to pressure fluctuations. When applying this model to a LES simulation, the SGS fluctuations of pressure increase the inception pressure to a certain level depending on the SGS turbulence intensity. All panels are shown as function of R_0 with different combinations of constant Re_λ and ε. Lower Re_λ and ε follow similar trends to those observed here, with overall smaller maximum f_{cav} rates. The stability limit for unbound growth of the nuclei is shown in the top left panel. Values to the left and above that curve, corresponding to low pressure where massive cavitation occurs, cannot be properly simulated, and instead are extended linearly from the valid points outside the curve. The exact shape of this extension is not

critical for the estimation of cavitation inception, which will happen when the first nuclei start cavitating. The contours shown in Fig. 6 are limited to a low threshold of 0.032 events/sec (about two events per minute). The overall trends are of stronger dependence on reference pressure than nuclei radius, except at very small radii, for which cavitation does not occur, and the occurrence of cavitation at higher reference pressure for increased Re_λ and ε. The dependence of f_{cav} with P_0 is exponential, with a slower decay at higher dissipation rates. Figure 7 demonstrates this dependence for a nuclei size of $R_0 = 35$ microns for $Re_\lambda = 22 - 240$. The cavitation events occur at considerably lower pressures at lower dissipation rates. Comparing cavitation events for $Re_\lambda = 240$, the onset of cavitation occurs at reference pressures of approximately 5, 10, and 25 kPa respectively for $\varepsilon = 10, 100,$ and 1000 m^3/s. This trend holds for cavitation events at other Reynolds numbers and nuclei sizes. At very low dissipation rates, all the curves almost coincide and there is no considerable sub-grid fluctuation correction in pressure for inception. This cavitation event rate f_{cav} database is used to determine the SGS cavitation event rate for any local CFD cell using multilinear interpolation in the four dimensional $(Re_\lambda, R_0, \log(\varepsilon), P_0)$ space. Notice that we access the database with R_{atm} and not with R_0. However, knowing P_0 and p_{atm}, one can compute R_0 from R_{atm} and vice versa. Analogously, for a fixed Re_λ, the variable ε can be replaced by u' and vice versa.

Table 1. Conditions and range of parameters for solving Rayleigh-Plesset equation to obtain the cavitation event rates.

Variables	Values/Range
Re_λ	22, 35, 55, 90, 150, 240
R_0^*	0, 0.025, 0.05, 0.10, 0.15, 0.2
ε (m^2/s^3)	0.001, 0.01, 0.1, 1, 10, 100, 1000
P_0 (kPa)	0-30

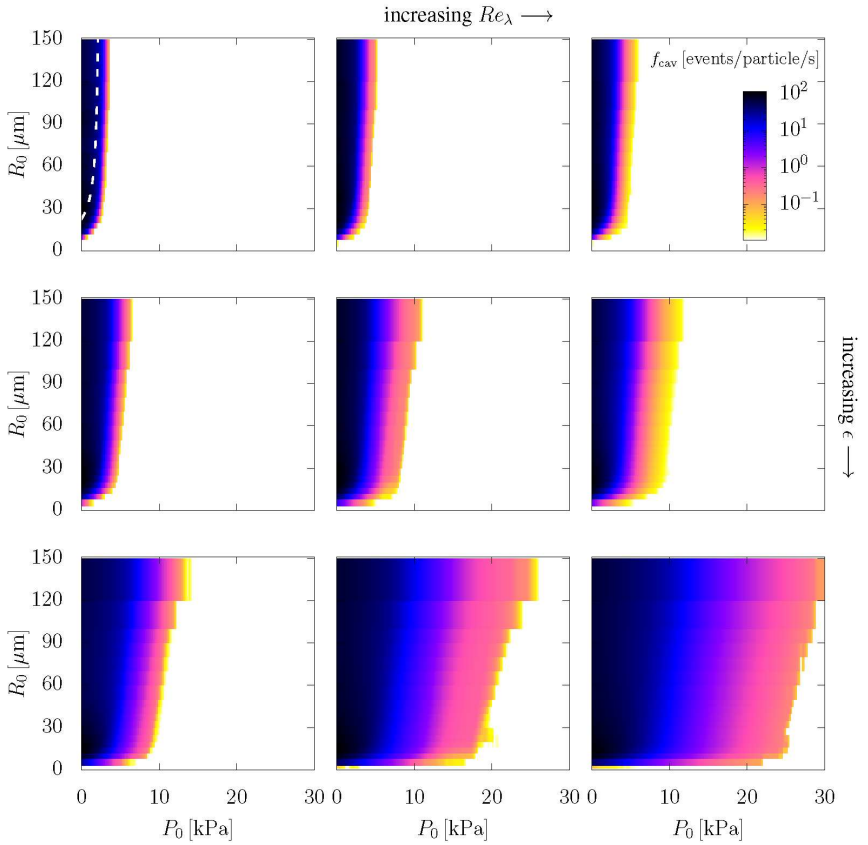

Figure 6. Cavitation event rates, f_{cav}, against reference pressure, P_0 and nuclei sizes R_0. Turbulent kinetic energy dissipation rates are respectively $10, 100,$ and 1000 m^3/s for the top, center, and bottom rows; Re_λ is $90, 150,$ and 240 for left to right columns. Blake's threshold for unbounded growth (with $p_{vap} = 2340$ Pa, $P_0 = 10$ kPa, $S = 7 \times 10^{-2}$ Pa-m, and $\gamma = 1.4$) is shown in the top left panel as a dashed line.

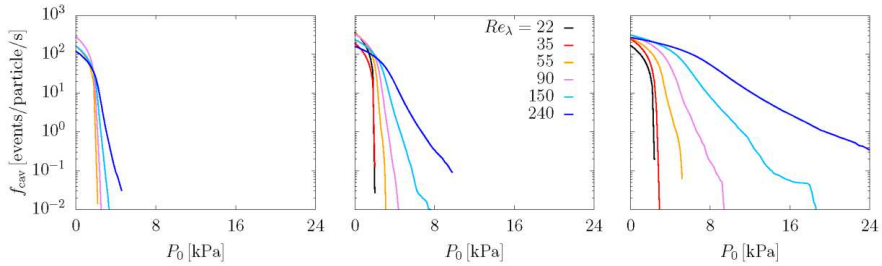

Figure 7: The variation of f_{cav} with P_0 at different Re_λ (colored lines) and at different turbulent kinetic energy dissipation rates (from left to right: $\varepsilon = 10, 100,$ and 1000 m^3/s) for nuclei of size $R_0 = 35$ microns (at atmospheric pressure).

2.2 Implementation for the Smagorinsky LES model

The necessary quantities to compute the local cavitation rate $F_{cav}(Re_\lambda, u', R_0, P_0)$ at every grid point, Re_λ, u', and P_0 are obtained from a CFD solution, with Re_λ and u' resulting from the SGS turbulence model. The other quantity, R_0, is independent of the CFD model. Three important assumptions are introduced at this point:

1) The SGS turbulence can be represented with HIT.
2) The SGS turbulence is fully developed, so statistically stationary HIT solutions can be used at the SGS level, and
3) Nuclei present in the cell are subject to the SGS turbulence long enough to enable use of cavitation bubble growth statistics obtained in §2.1.

These assumptions must be considered in a Lagrangian sense, since both nuclei and turbulent structures are transported with the flow, and thus the residence time of nuclei in a patch with certain turbulence properties depends mostly on the formation, evolution, and decay time of the resolved turbulent structures. A high turbulence patch may be passing through a given cell at a particular time step, but that same patch followed an upstream trajectory and will continue in a downstream trajectory changing turbulence properties within several time steps, since a proper LES computation resolves the slower larger scales and models the fast-changing smaller scale.

2.2.1 Sub-grid scale turbulence in LES

The two natural independent parameters to obtain the pressure history of HIT are the Taylor Reynolds number, which controls the intensity of the SGS turbulence, and the SGS velocity fluctuations u', used to dimensionalize the dimensionless pressure obtained in HIT. The SGS velocity fluctuations are obtained from the SGS TKE k_s, while the SGS TKE dissipation rate is related to Re_λ and u' since $Re_\lambda = u'^2 \sqrt{\frac{15}{\nu \varepsilon_s}}$. We choose k_s and ε_s as the main parameters since they

are more intuitive than other possible pairs of independent parameters, like the strain rate magnitude S or the Taylor Reynolds number.

The simplest zero-equation LES SGS model is the Smagorinsky model (Smagorinsky 1963), where the proposed length scale is a fraction of the grid cell size $\overline{\Delta} = (\Delta_x \Delta_y \Delta_z)^{1/3}$

$$l = C_S \overline{\Delta} \tag{16}$$

and the velocity scale is computed from the absolute filtered strain rate $\overline{\mathrm{S}} = \sqrt{2\overline{\mathrm{S}}_{ij}\overline{\mathrm{S}}_{ij}}$ and the length scale to yield a turbulent viscosity based on Prandtl (1925) mixing length hypothesis

$$\nu_t = (C_S \overline{\Delta})^2 \overline{\mathrm{S}} \tag{17}$$

The strain rate of the filtered flow is $\overline{\mathrm{S}}_{ij} = \frac{1}{2}(\frac{\partial \overline{u}_i}{\partial x_j} + \frac{\partial \overline{u}_j}{\partial x_i})$ and for HIT the Smagorinsky constant is $C_s = 0.16$ (Lilly 1967), though in general, the optimum value is flow-dependent. The SGS TKE dissipation rate is computed as

$$\varepsilon_s = \nu_t \overline{\mathrm{S}}^2 = (C_S \overline{\Delta})^2 \overline{\mathrm{S}}^3 \tag{18}$$

Other zero-equation SGS models, for instance the dynamic Smagorinsky model of Germano et al. (1991) and modification of Lilly (1992) or the gradient model of Clark et al. (1979), produce different eddy viscosities that can be combined with Eq. (18) to obtain the TKE dissipation rate. While in CFD it is appropriate to maintain consistency in the turbulence model used with the methodology to compute the TKE dissipation, Eqs. (17) and (18) provide a formulation to obtain estimates for any LES computation and have been used even in experimental velocity fields (Sheng et al. 2000, Bertents et al. 2015).

Of critical importance is an appropriate estimation of the intermittency, as pressure fluctuations trigger inception. Cerutti and Meneveau (1998) showed that the Smagorinsky and the volume-averaged dynamic Smagorinsky models predict realistic levels of intermittency in HIT, while the local dynamic Smagorinsky model produces much more intermittency than the true SGS dissipation field.

The TKE at the SGS level can be estimated assuming a Kolmogorov spectrum as

$$k_S = \int_{\pi/\overline{\Delta}}^{\infty} C \varepsilon^{2/3} \kappa^{-5/3} d\kappa = \frac{3}{2} C (\frac{\varepsilon \overline{\Delta}}{\pi})^{2/3} \tag{19}$$

Equation (19) is consistent with the expression used in the SGS TKE equation to estimate the dissipation rate (Kim and Menon 1997)

$$\frac{\partial k_S}{\partial t} + \overline{u}_i \frac{\partial k_S}{\partial x_i} = -\overline{\tau}_{ij} \frac{\partial \overline{u}_i}{\partial x_j} - \varepsilon_S + \frac{\partial}{\partial x_i}(\nu_t \frac{\partial k_S}{\partial x_i}) \tag{20}$$

where the SGS TKE dissipation is modeled as $\varepsilon_S = C_\varepsilon k_S^{3/2}/\overline{\Delta}$, and the constant is $C_\varepsilon \cong 1.0$ (Chumakov 2007). An equivalent expression is obtained if in Eq. (19) we use the Kolmogorov constant $C = 1.5$, resulting in

$$k_S = \frac{3}{2\pi^{2/3}} C(\varepsilon\overline{\Delta})^{2/3} = 1.05(\varepsilon\overline{\Delta})^{2/3} \tag{21}$$

Notice that Eq. (20) uses the SGS TKE dissipation rate ε_S and Eq. (21) the total TKE dissipation rate ε. We use the additional assumption that the LES resolution is such that the resolved TKE dissipation rate is negligible, such that $\varepsilon_S = \varepsilon$. Notice also that if a zero-equation model is used then the SGS turbulence quantities in Eqs. (18) and (21) are derived from the resolved shear rate $\bar{S}$ only. Ultimately this means that the SGS Re_λ and u' depend on one CFD parameter and the grid size. One-equation LES approaches solving an equation for the SGS TKE like Eq. (20) result in k_S independent of the local shear rate, but the TKE dissipation is still linked to k_S through Eq. (21), as local equilibrium is assumed. While for Smagorinsky and other zero-equation models only one parameter controls the SGS turbulence, more advanced SGS models can provide the two independent parameters needed to characterize the SGS cavitation rate and inception.

The Taylor Reynolds number (Eq. (1)) is based on the SGS velocity fluctuations, computed from Eq. (21) as

$$u' = \sqrt{\frac{2}{3} k_S} \tag{22}$$

Combining Eqs. (1), (18), and (21) and using $\lambda = u'\sqrt{15\nu/\varepsilon}$ yields

$$Re_\lambda = \frac{\sqrt{15}}{\pi^{2/3}} C\overline{\Delta}^{2/3} \sqrt{\frac{\varepsilon^{1/3}}{\nu}} = 2.71\overline{\Delta}^{2/3} \sqrt{\frac{\varepsilon^{1/3}}{\nu}} \tag{23}$$

If a Smagorinsky model is used, plugging Eq. (18) into Eq. (23) results in a final expression for Re_λ

$$Re_\lambda = \frac{\sqrt{15} C {C_s}^{1/3}}{\pi^{2/3}} \overline{\Delta} \sqrt{\frac{\bar{S}}{\nu}} = 1.47\overline{\Delta} \sqrt{\frac{\bar{S}}{\nu}} \tag{24}$$

Similarly, using Eqs. (1), (18) and (21) the SGS velocity fluctuations are

$$u' = \frac{C^{1/2} {C_s}^{2/3}}{\pi^{1/3}} \overline{\Delta} S = 0.247\overline{\Delta}\bar{S} \tag{25}$$

From any CFD solution providing $\bar{S}$, u' and Re_λ are computed from Eqs. (24) and (25) using the Smagorinsky model. If a different SGS model is used then ε can be computed directly from the SGS υ_t using Eq. (18), then use Eqs. (1), (22) and (23) to compute u' and Re_λ.

2.3 Finding the cavitation number at inception and inception location

Once SGS turbulence quantities Re_λ, u', and the local absolute pressure p_{abs} are obtained for every grid point in the CFD computation, the cavitation rate at every grid point for each nuclei size R_0 can be computed from the database $f_{cav}(Re_\lambda, u', R_0, p_{abs} + p_{ref})$, that is, accessing the database with $P_0 = p_{abs} + p_{ref}$, where p_{ref} is a floating reference pressure used to define the cavitation number $\sigma = (p_{ref} - p_{vap})/(0.5\rho U_0^2)$ and p_{abs} is the absolute pressure for the solution

at $p_{ref} = 0$. The cavitation rate density at p_{ref} in events/m^{3}s is also an instantaneous field variable computed at every grid point and time step

$$F_{cav}(\boldsymbol{x}, t, p_{ref}) = \int_0^\infty N(R_0) f_{cav}(Re_\lambda, u', R_0, p_{abs} + p_{ref}) dR_0 \tag{26}$$

where the nuclei size distribution $N(R_0)$ is a property of the fluid. Implementation of Eq. (26) requires efficient numerical integration of the discretized nuclei size distribution and a fast lookup table for the local cavitation rate since it is computed for every grid point at every time step for each reference pressure. This is better done as a post-processing step since several reference pressures need to be evaluated to find the cavitation inception pressure.

The cavitation inception pressure and location are obtained after defining an observable cavitation rate for the case considered, then changing the reference pressure until the observable rate is achieved. For example, in visual cavitation the observable rate could be one cavitation event every 10 s in an observation volume V. In such a case, the inception pressure, $P_{inception}$, is defined as the reference pressure p_{ref} that satisfies

$$\frac{1}{T}\int_0^T \int_V F_{cav,V}(\boldsymbol{x}, t, p_{ref}) d\boldsymbol{x} dt = 0.1\ Hz \tag{27}$$

The corresponding inception cavitation number is $\sigma_i = (P_{inception} - p_{vap})/(0.5\rho U_0^2)$ and the inception location is obtained finding the position with the maximum time-averaged cavitation rate,

$$\bar{F}_{cav,V}(\boldsymbol{x}, p_i) = \frac{1}{T}\int_0^T F_{cav,V}(\boldsymbol{x}, t, p_i) dt \tag{28}$$

3. Model Validation in homogeneous isotropic turbulence

3.1. LES HIT Solver

For LES computation of HIT flow, the same spectral code that has been described in §2.1.1. was used. The flow evolves following Eqs. (2) and (3), however u_i and p are the coarse-grained velocity vector and pressure in the case of LES, and the stress term τ_{ij} now includes additional SGS values and is written as

$$\tau_{ij} = 2(\nu + \nu_t) S_{ij}, \tag{29}$$

where, ν_t is the Smagorinsky model eddy viscosity as discussed in §2.2.1.

3.2 LES solutions and predicted pressure pdf

Homogeneous isotropic turbulence is a spatially or temporal concept, not necessarily applicable at the subgrid scale level. While long term statistics at a point can show that the turbulence is isotropic, short term behavior can be highly anisotropic, for instance as a result of a large-scale vortex causing local shear. To evaluate how closely the assumption of local HIT

conditions matches the pressure pdf, we compare the model performance for a LES computation to the DNS prediction of the Lagrangian pressure pdf at $Re_\lambda = 240$ and 324. LES computations are performed using grids with 64^3 grid points, much coarser than DNS.

The pressure pdf at the subgrid scale is a function of the dimensionless pressure fluctuations $p'/\rho u'^2_{sgs}$ and Re_λ. In a LES computation at every grid point and time step we have a pressure p_{LES} respect to the average pressure. The local, instantaneous pressure pdf is then

$$pdf[(p_{LES} + p'\rho u'^2_{sgs})/\rho u'^2), \boldsymbol{x}, t] = pdf_{sgs}(Re_\lambda, p'/\rho u'^2_{sgs}, \boldsymbol{x}, t) \tag{30}$$

The total pdf is computed by integrating Eq. (30) in time and space for the LES computational domain. Discretization into bins of $(p_{LES} + p'\rho u'^2_{sgs})/\rho u'^2)$ determines values of $p'/\rho u'^2_{sgs}$ for each bin, and the pdf is computed filling the bins for each spatial point at each time step.

Instantaneous solutions colored with pressure for LES and DNS are shown in Fig. 8. Results comparing the pressure pdf's for LES plus the SGS model and DNS are shown in Fig. 9. With the strain rate computed using the grid spacing h the lower pressures present in the pressure pdf are underestimated. Computing all parameters in Eqs. (20)-(24) with wider grid spacing increases the SGS pressure fluctuations. It was determined through tests that a spacing $2\bar{\Delta}$ yields the best results, properly predicting the pressure pdf for $-20 < p < 5$, the region where occurrence of cavitation events is most important, since lower pressures are less likely and of shorter duration. This level of correction is significant and leads to the speculation that using HIT at the SGS level underestimates the pressure fluctuations, and that possibly HST is more appropriate to develop the SGS model.

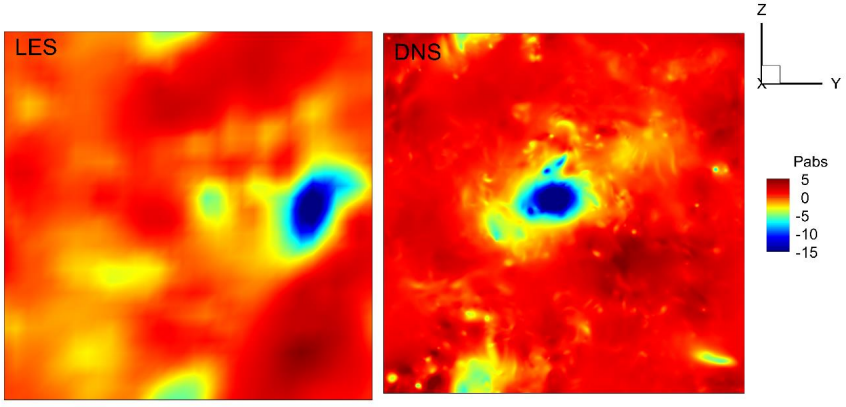

Figure 8: Instantaneous pressure solutions for $Re_\lambda = 240$ computed with LES (left) and DNS (right).

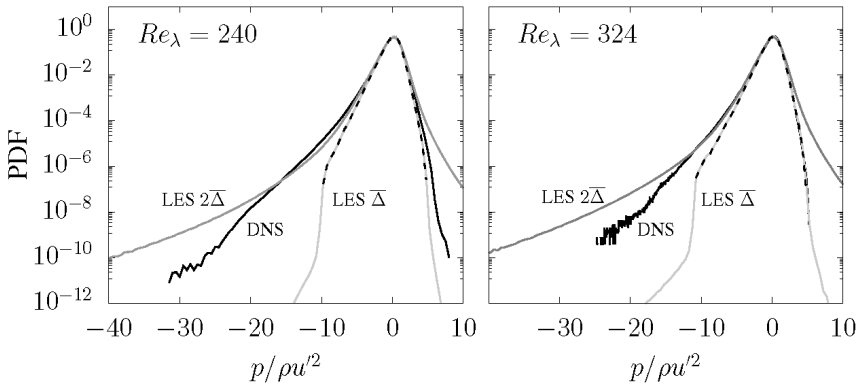

Figure 9: HIT pressure probability density functions for LES and DNS at $Re_\lambda = 240$ and 324, dashed lines represent the pressure pdfs of LES without any correction. The proposed SGS model best corrects the pressure pdfs using a grid spacing of $2\overline{\Delta}$.

3.3 Comparison against experimental data

The methodology was tested against the experimental data of Laporta et al. (2000), who studied cavitation in homogeneous isotropic turbulence produced with counter-rotating disks. The disks produced a region in the volume of the experimental apparatus with TKE dissipation between 2.03 and 4.12 m^2/s^3 and $Re_\lambda = 1660, 1772$ and 1880. These conditions were simulated with the forced HIT spectral code described in §3.1 (LES model) with grids of 256^3 grid points for all Re_λ, and for three grids (192^3, 256^3, and 384^3) for $Re_\lambda = 1772$. The nuclei number density is not reported in the experiments, so a generic nuclei size distribution (Li and Carrica 2021) was used with 1×10^6 bubbles/m^3.

Time histories of the minimum dimensionless pressure predicted with LES are shown in Fig. 10 for three grids at $Re_\lambda = 1772$. Results show that, as expected, the minimum pressure excursions are more violent as the grid is refined. Since the corrections for SGS pressure fluctuations decrease as the grid is refined, the final cavitation rate (due to resolved pressure plus SGS model) should stay constant for all grids.

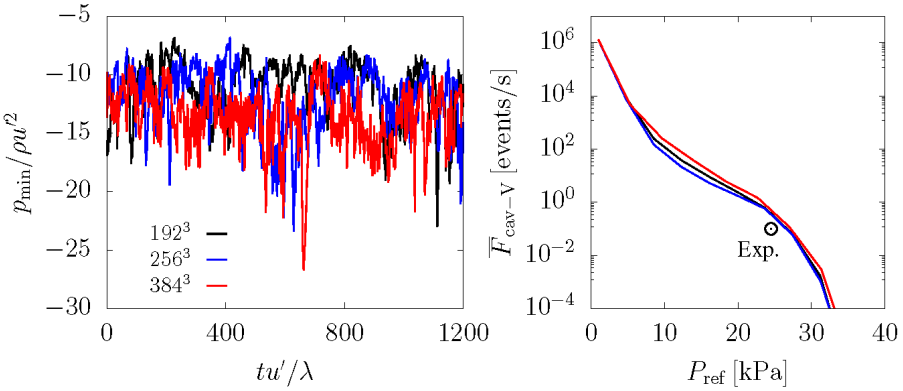

Figure 10: Time history of minimum pressure for LES of HIT at $Re_\lambda = 1772$ for grids with 192^3, 256^3, and 384^3 grid points (left), and corresponding cavitation event rate including the experimental point (right).

Figure 10 also shows the total cavitation frequency in events/s observed in a 3 cm^3 volume, as used in the experiment to determine cavitation. As the pressure is reduced this cavitation frequency quickly increases, and cavitation becomes detectable when the frequency is 0.1 Hz. Note that the model predicts similar cavitation inception point for all grids. The classic method to predict cavitation inception based on the minimum pressure obtained in CFD results in an underestimation of the inception pressure, as shown in Fig. 11, though as the grid is refined the results improve.

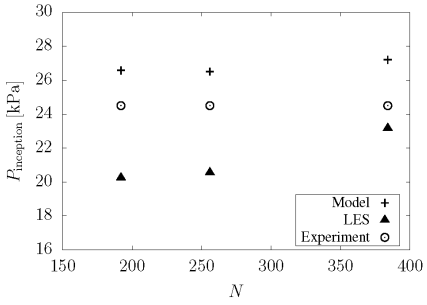

Figure 11: Predicted cavitation inception pressure for LES of HIT at $Re_\lambda = 1772$ for cases with N^3 grid points, with $N = 192, 256$ and 384.

The cavitation inception predicted by the model at three Taylor scale Reynolds numbers are shown in Fig. 12. The turbulence-induced pressure fluctuations increase as the Reynolds number increases, resulting in cavitation inception at higher pressures. The predicted cavitation frequency also quickly increases for a given pressure. As an example, at 25,000 Pa the frequency is 1×10^{-5} for $Re_\lambda = 1660$, increasing to 3×10^{-1} at $Re_\lambda = 1772$ and 20 times more for $Re_\lambda = 1880$. The minimum pressures predicted by LES reach lower values as Re_λ increases, see Fig. 13. The model tends to overpredict the cavitation inception pressure by approximately 1.5 KPa, though this number may be lower or higher as the cavitation inception pressure in the experiments has not been explicitly reported and was estimated based on experimental plots of event rate.

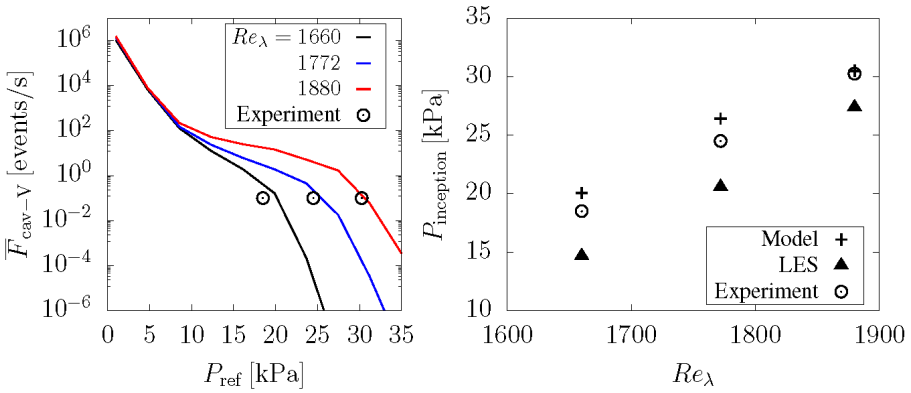

Figure 12: Predicted cavitation inception pressure by the model for LES of HIT at $Re_\lambda = 1660, 1772$ and 1880. Cavitation rate (left) and inception pressure (right).

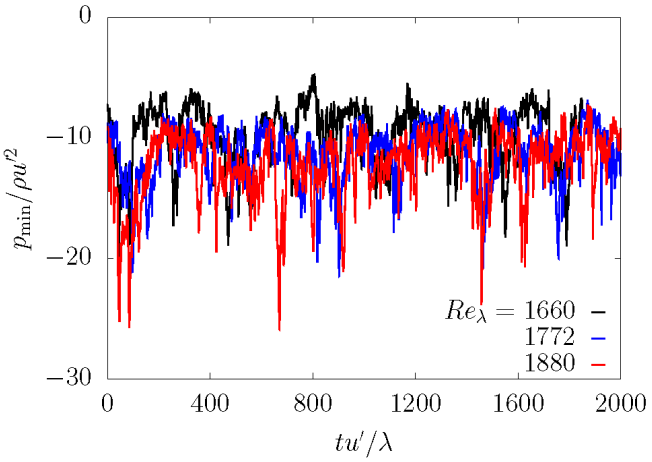

Figure 13: Minimum pressure histories predicted with LES of HIT for $Re_\lambda = 1660, 1772,$ and 1880.

4. Conclusions, limitations, and further discussion

We presented a sub-grid scale model of cavitation inception that accounts for unresolved SGS pressure fluctuations assuming that the SGS turbulent flow is homogeneous and isotropic. Cavitation rates are obtained by simulating DNS Lagrangian transport of nuclei of different sizes in HIT at various Re_λ to obtain pressure histories experienced by the nuclei. Then the Rayleigh-Plesset equation at different reference pressures is solved for all the nuclei sizes and velocity fluctuations, recording bubble growth events that reach bubble sizes above 0.5 mm to obtain tables for the local cavitation rate. The cavitation rate of an LES simulation is obtained by computing the local SGS turbulence quantities and entering the cavitation rate tables with the local nuclei size distribution and cell pressure. Lowering the reference pressure increases the cavitation rate, which reaches inception when the cavitation events are observable at one cavitation event every 10 seconds in a problem-dependent visual volume.

The strongest assumption in the model is the hypothesis of homogeneous isotropic turbulence at the SGS level. The use of forced HIT to compute the SGS cavitation rate results in the unresolved turbulence to depend only on the resolved strain rate. It is reasonable to assume that the local SGS turbulence will be a result of local production and destruction, as well as transport. For instance, there could be considerable SGS turbulence as a result of transport from a nearby high-turbulence spot, even with a zero local strain rate; the opposite condition of considerable production due to high local strain rate but low SGS turbulence is also possible, and not accounted for in our approach. More discussion on this point is provided in §4.1.

We can expect the model to provide a level of correction to the cavitation inception predicted using the lowest pressures resolved by LES, resulting in cavitation at higher pressures. The correction will be stronger in cases of higher turbulence and lower reference pressures, it will also increase as the grids are coarser and the fraction of unresolved turbulence increases. The model will provide little or no correction for flows with weak or suppressed turbulence, as expected. Notice that a good estimate of the unresolved turbulence is necessary.

The inception of cavitation also depends on the water quality, which has a prominent effect on the nuclei concentration, size distribution, presence of non-condensable gases and of surfactants. Our model is sensitive to the first two factors through the nuclei size distribution function $N(R_0)$ in Eq. (26). Although current computations are based on a uniform distribution of nuclei in the free stream as an input, it is possible to transport the distribution function during the CFD computation to account for increased concentration of larger nuclei in lower pressure regions. Work to expand the cavitation inception model to account for non-condensable gases and surfactants is currently starting.

Another critical parameter influencing the inception point is the cavitation inception criterion, as discussed earlier. We are in the process of studying the sensitivity to different acoustic and visual cavitation inception criteria, as video recording instead of visual observation is presently more accurate and capable of detecting smaller bubbles. The criterion of observable $1\,mm$ diameter bubbles used in this paper results in a void fraction of 0.05% for a nuclei concentration

of 10^6 nuclei/m^3. This criterion can be used in a homogeneous mixture model (without any SGS cavitation inception model).

4.1 Using HST instead of HIT

While HIT provides pressure statistics for cavitation inception modeling that can be used to evaluate SGS pressure fluctuations (Bappy et al. 2020b), it can be argued that HST is a more appropriate choice. In particular, passive scalar transport in turbulent flows shows a persistent anisotropy at all scales independent of the Reynolds number (Warhaft 2000). Pumir (1996) showed that HST exhibits small scale anisotropy in the direction of the imposed vorticity even for high Reynolds numbers. In addition, HST exhibits high enstrophy and TKE fluctuations that can lead to higher pressure fluctuations than those occurring in HIT, as evidenced by strong vortical structures reminiscent of those in turbulent channels and boundary layers (Pumir 1996, Dong et al. 2017). In this work we restrict our analysis to HIT, though the framework can be easily extended to HST should proper statistics of pressure for transported nuclei become available. Current and future work is focusing on improving the SGS cavitation inception model by exploring HST and transport models to estimate the SGS turbulence. Preliminary results show that, for the same Re_λ, HST produces more pressure fluctuations than HIT and reaches lower pressures more frequently.

4.2 Extension of the inception model to RANS

Unsteady RANS solutions resolve only the largest structures, if any. The SGS turbulence is therefore all modeled. RANS grids are frequently considerably coarser than LES grids, thus the local isotropy and homogeneity assumptions are likely violated. Yet, a correction for cavitation at the SGS level can be developed following the same procedures as in LES accepting that the SGS turbulence is misrepresented. The SGS velocity fluctuations and Taylor Reynolds number are

$$u'^2 = \frac{2k}{3} \tag{31}$$

$$Re_\lambda = \frac{2.582k}{\sqrt{\upsilon\varepsilon}} = 8.61\sqrt{\frac{\upsilon_t}{\upsilon}} \tag{32}$$

where k and ε are obtained directly from the turbulence model local quantities. Notice that, in contrast to LES, the SGS turbulence in RANS is independent of the grid size, assuming that the CFD solution converged in grid. In addition, because all turbulence is modeled, the SGS Re_λ and u' will be large compared to LES. Ship boundary layers with length-based Reynolds numbers in excess of 10^9 can reach $\upsilon_t/\upsilon \cong 100{,}000$, implying $Re_\lambda \approx 3{,}000$. More common conditions excluding boundary layers exhibit $\frac{\upsilon_t}{\upsilon} < 3{,}000$, which results in $Re_\lambda < 500$. Computing HIT for $Re_\lambda \cong 400$ requires 1024^3 domains (Cardesa et al. 2017), 8 times more than the 512^3 used for the maximum $Re_\lambda = 240$ used herein and reaching $Re_\lambda \cong 500$ will likely require a 2048^3

computational domain or bigger. These computations would be expensive but are doable, this is also part of our future focus.

Acknowledgements

This research was supported by the Office of Naval Research grants N00014-17-1-2676 (University of Minnesota lead institution) and N00014-20-1-2553, with Dr. Ki-Han Kim as program officer. LSF and GCB acknowledge support from CNPq and FAPESP (Brazil).

References

Anton, I., "The effects of turbulence on cavitation inception," *La Houille Blanche* **5**, 315-322 (1993)

Arndt, R.E., "Cavitation in vortical flows," *Annu. Rev. Fluid Mech.* **34**, 143–175 (2002)

Arndt, R.E., and George, W.K., "Pressure fields and cavitation in turbulent shear flows," *12th Symp. Naval Hydrodynamics*, 327-339 (1979)

Asnaghi, A., Svennberg, U., and Bensow, R. E., "Numerical and experimental analysis of cavitation inception behaviour for high-skewed low-noise propellers," *Appl. Ocean Res.* **79**, 197-214 (2018)

Balachandar, S., and Eaton, J.K., "Turbulent dispersed multiphase flow," *Annu. Rev. Fluid Mech.* **42**, 111–133 (2010)

Bappy, M., Martin, J. E., Li, J., Buscaglia, G. C., and Carrica, P. M., "A stochastic approach to cavitation inception prediction," *6th Int. Symp. Marine Propulsors*, 91-98, (2019a)

Bappy, M.H., Carrica, P.M., and Buscaglia, G.C., "Lagrangian statistics of pressure fluctuation events in homogeneous isotropic turbulence," *Phys. Fluids* **31**, 085111 (2019b)

Bappy, M.H., Vela-Martín, A., Buscaglia, G.C., Carrica, P.M., and Freire, L.S., "Effect of bubble size on Lagrangian pressure statistics in homogeneous isotropic turbulence," *J. Phys.: Conf. Ser.* **1522**, 012002 (2020a)

Bappy, M.H., Carrica, P.M., Vela-Martín, A., Freire, L.S., and Buscaglia, G.C., "Pressure statistics of gas nuclei in homogeneous isotropic turbulence with an application to cavitation inception," *Phys. Fluids* **32,** 095107 (2020b).

Bertents, G., van der Voort, D., Bocenagra-Evans, H., and van de Water, W., "Large-eddy estimate of the turbulent dissipation rate using PIV," *Exp. Fluids* **56**, 89 (2015).

Brandao, F. L., and Mahesh, K., "Large-eddy simulation of cavitation inception in a shear flow," *Int. J. Multiphase Flow* **146**, 103865 (2022).

Brennen, C.E., "Cavitation and bubble dynamics," Cambridge University Press, (1995).

Brennen, C., Colonius, T., Wang, Y.C., and Preston, A., "Cloud cavitation phenomena," *22nd Symp. Naval Hydrodynamics*, 239-253 (1999).

Cao, N., Chen, S., and Doolen, G.D., "Statistics and structures of pressure in isotropic turbulence. *Phys. Fluids* **11**, 2235–2250 (1999).

Cardesa, J.I., Vela-Martín, A., and Jiménez, J., "The turbulent cascade in five dimensions, *Science* **357** (6353), 782-784 (2017).

Cerutti, S., and Meneveau, C., "Intermittency and relative scaling of subgrid-scale energy dissipation in isotropic turbulence," *Phys. Fluids* **10**, 928 (1998).

Chen, L., Zhang, L., Peng, X., and Shao, X., "Influence of water quality on the tip vortex cavitation inception," *Phys. Fluids* **31**, 023303 (2019).

Cheng, H., Long, X., Ji, B., Peng, X., and Farhat, M., "A new Euler-Lagrangian cavitation model for tip-vortex cavitation with the effect of non-condensable gas," *Int. J. Multiphase Flow* **134**, 103441 (2021).

Chumakov, G., "Scaling properties of subgrid-scale energy dissipation," *Phys. Fluids* **19**, 058104 (2007).

Clark, R.A., Ferziger, J.H., and Reynolds, W.C., "Evaluation of subgrid-scale models using an accurately simulated turbulent flow," *J. Fluid Mech.* **91**, 1-16 (1979).

Dong, S., Lozano-Duran, A., Sekimoto, A., and Jimenez, J., "Coherent structures in statistically stationary homogeneous shear turbulence," *J. Fluid Mech.* **816**, 167-208 (2017).

Ezzatneshan, E., "Study of surface wettability effect on cavitation inception by implementation of the lattice Boltzmann method," *Phys. Fluids* **29**, 113304 (2017).

Germano, M., Piomelli, U., Moin, P., and Cabot, W.H., "A dynamic subgrid scale eddy viscosity model," *Phys. Fluids A* **3**, 1760–1765 (1991).

Gotoh, T., and Rogallo, R. "Intermittency and scaling of pressure at small scales in forced isotropic turbulence," *J. Fluid Mech.* **396**, 257–285 (1999).

Hsiao, C.T., and Pauley, L., "Study of Tip Vortex Cavitation Inception Using Navier-Stokes Computation and Bubble Dynamic Model," *J. Fluids Eng.* **121**, 198–204 (1999).

Hsiao , C., Chahine, G. L., and Liu, H., "Scaling Effect on Prediction of Cavitation Inception in a Line Vortex Flow ." ASME. *J. Fluids Eng*. **125**, 53–60 (2003).

Hsiao, C.T., and Chahine, G., "Prediction of tip vortex cavitation inception using coupled spherical and nonspherical bubble models and Navier–Stokes computations," *J. Marine Sci. Technol.* **8**, 99-108 (2004).

Joseph, D. D., "Cavitation and the state of stress in a flowing liquid," *J. Fluid Mech.* **366**, 367-378 (1998).

Kim, W.W., and Menon, S., "Application of the localized dynamic subgrid-scale model to turbulent wall-bounded flows," 35th Aerospace Sci. Meeting and Exhibit (AIAA paper 97-0210) (1997).

Kodama, Y., Take, N., Tamiya, S., and Kato, H., "The Effects of Nuclei on the Inception of Bubble and Sheet Cavitation on Axisymmetric Bodies," *J. Fluids Eng.* **103**, 557–563 (1981).

Kolmogorov, A.N., "A refinement of previous hypotheses concerning the local structure of turbulence in a viscous incompressible fluid at high Reynolds numbers," *J. Fluid Mech.* **13**, 82-85 (1962).

La Porta, A., Voth, G., Moisy, F., and Bodenschatz, E., "Using cavitation to measure statistics of low-pressure events in large Reynolds number turbulence," *Phys. Fluids* **12**, 1485 (2000).

Li, J., "Contributions to modeling of bubble entrainment for ship hydrodynamics applications," PhD Thesis - *The University of Iowa* (2015).

Li, J., Castro, A.M., and Carrica, P.M., "A pressure–velocity coupling approach for high void fraction free surface bubbly flows in overset curvilinear grids," *International Journal for Numerical Methods in Fluids* **79(7)**, 343-69 (2015).

Li, J., and Carrica, P.M., "A population balance cavitation model," *International Journal of Multiphase Flow* **138**, 103617 (2021).

Lilly, D.K., "The representation of small-scale turbulence in numerical simulation experiments," Proc. IBM Sci. Computing Symposium on Environmental Science, 195 (1967).

Lilly, D.K., "A proposed modification on the Germano subgrid-scale closure method," *Phys. Fluids A* **4**, 633–635 (1992).

Meyer, R.S., Billet, M., and Holl, J., "Freestream Nuclei and Traveling Bubble Cavitation," *J. Fluids Eng*. **114**, 672–679 (1992).

Mørch, K.A., "Cavitation inception from bubble nuclei," *Interface Focus* **5**, 20150006 (2015).

Okabayashi, K., & Kajishima, T., "Modeling of the subgrid-scale pressure distribution in turbulent mixing layer," *J. Fluid Sci. Tech.* **6**, 73-84 (2011).

Pumir, A,. "A numerical study of pressure fluctuations in three-dimensional, incompressible, homogeneous, isotropic turbulence," *Phys. Fluids* **6**, 2071–2083 (1994).

Pumir, A., "Turbulence in homogeneous shear flows," *Phys. Fluids* **8**, 3112 (1996).

Prandtl, L., "Bericht über Untersuchungen zur ausgebildeten Turbulenz," *Zeitschrift für Angewandte Mathematik und Mechanik* **5**, 136–139 (1925).

Ran, B., and Katz, J., "Pressure fluctuations and their effect on cavitation inception within water jets," *J. Fluid Mech.* **262**, 223-63 (1994).

Sheng, J., Meng, H., Fox, R.O., "A large eddy PIV method for turbulence dissipation rate estimation," *Chem. Eng. Sci.* **55**, 4423–4434 (2000).

Singhal, A.K., Athavale, M., Li, H., and Jiang, Y., Mathematical Basis and Validation of the Full Cavitation Model. *J. Fluids Eng.* **124**, 617-624 (2002).

Smagorinsky, J., "General circulation experiments with the primitive equations. I. the basic experiment," *Mon. Weather Rev.* **91**, 99-164 (1963).

Song, M., Xu, L., Peng, X., and Tang, D., "An acoustic approach to determine tip vortex cavitation inception for an elliptical hydrofoil considering nuclei-seeding," *Int. J. Multiphase Flow* **90**, 79-87 (2017).

Spalart, P.R., "Detached-eddy simulation," *Annu. Rev. Fluid Mech*. **41**:181-202 (2009).

Straka, W. A., Meyer, R. S., Fontaine, A. A., and Welz, J. P., "Cavitation inception in quiescent and co-flow nozzle jets," *J. Hydrodyn. Ser. B* **22**, 813-819 (2010).

Toschi, F., and Bodenschatz, E., "Lagrangian properties of particles in turbulence," *Annu. Rev. Fluid Mech*. **41**, 375–404 (2009).

Van Atta, C., "Local isotropy of the smallest scales of turbulent scalar and velocity fields," *Proc. R. Soc. London A* **434**, 139-147 (1991).

Wang, Y.C., "Effects of nuclei size distribution on the dynamics of a spherical cloud of cavitation bubbles," *J. Fluids Eng.* **121**, 881–886 (1999).

Warhaft, Z., "Passive scalars in Turbulent flow," *Annu. Rev. Fluid Mech*. **32**, 203-240 (2000).

Wimshurst, A., Vogel, C., and Willden, R., "Cavitation limits on tidal turbine performance," *Ocean Eng.* **152**, 223-233 (2018).

PLEASE CITE THIS ARTICLE AS DOI: 10.1063/5.0079313

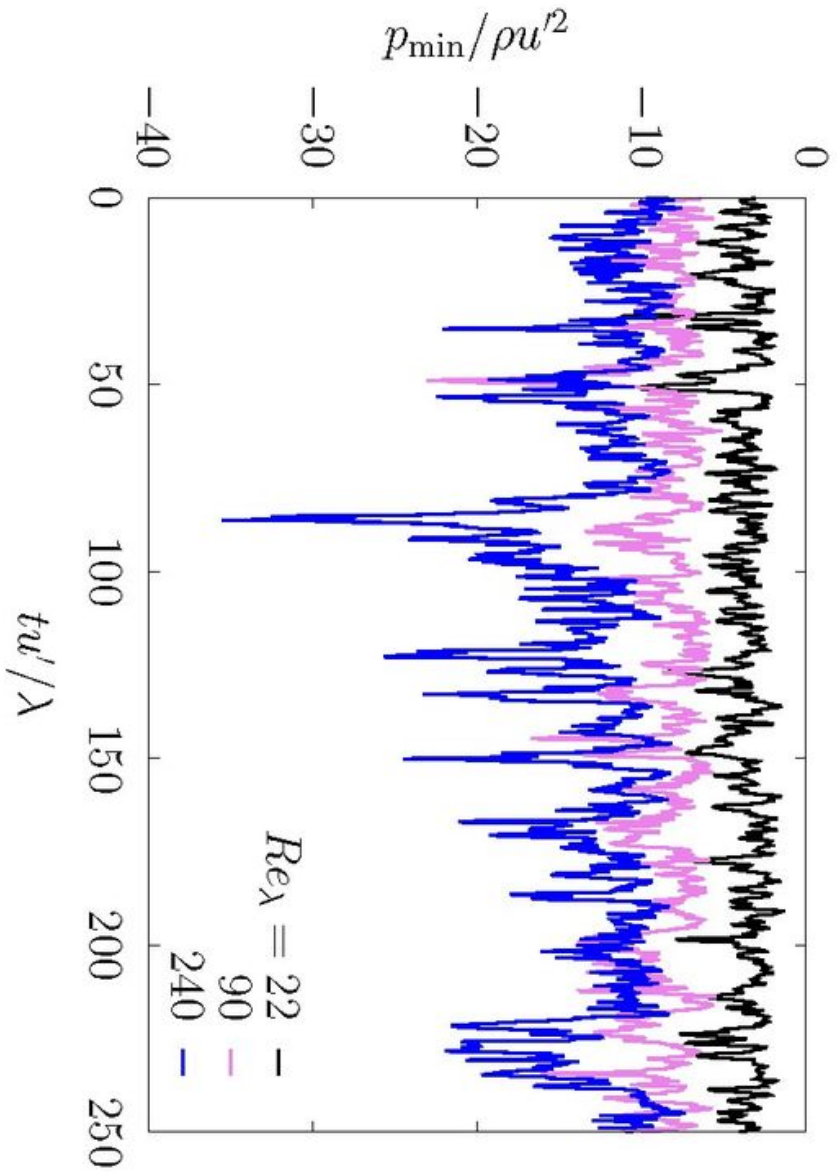

PLEASE CITE THIS ARTICLE AS DOI: 10.1063/5.0079313

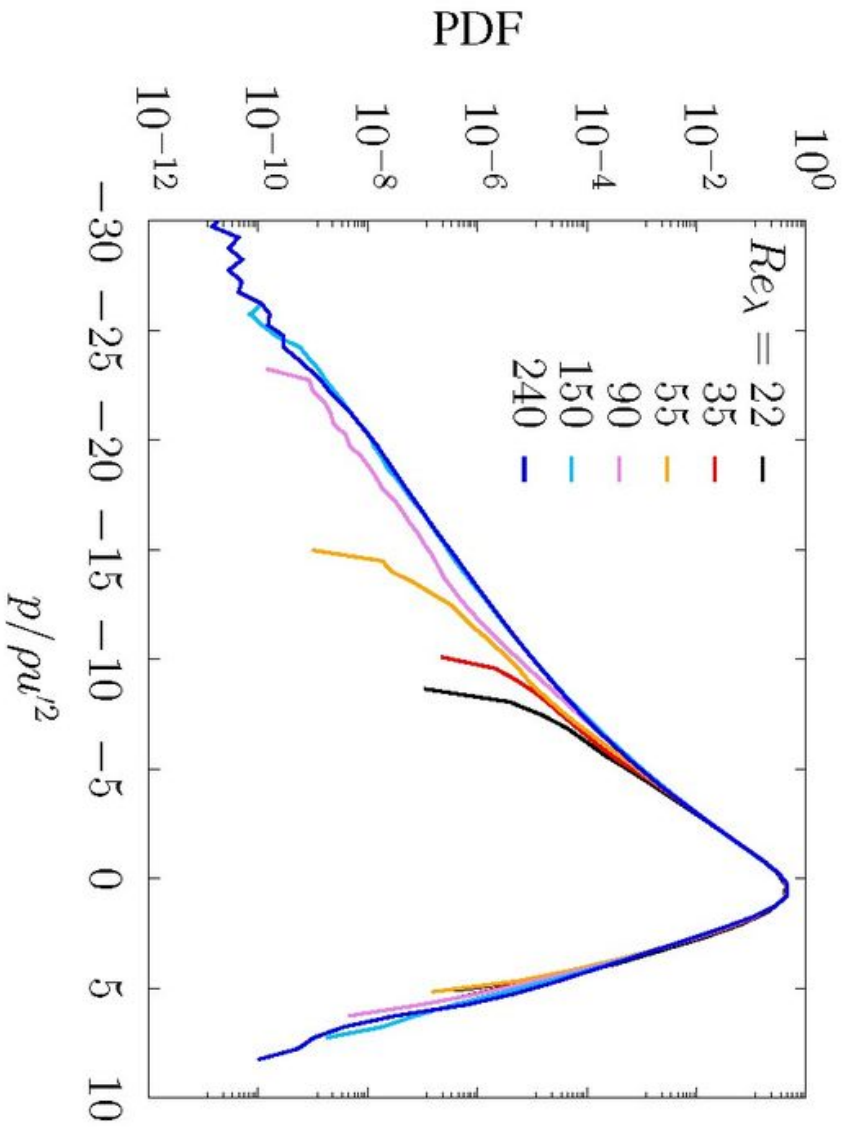

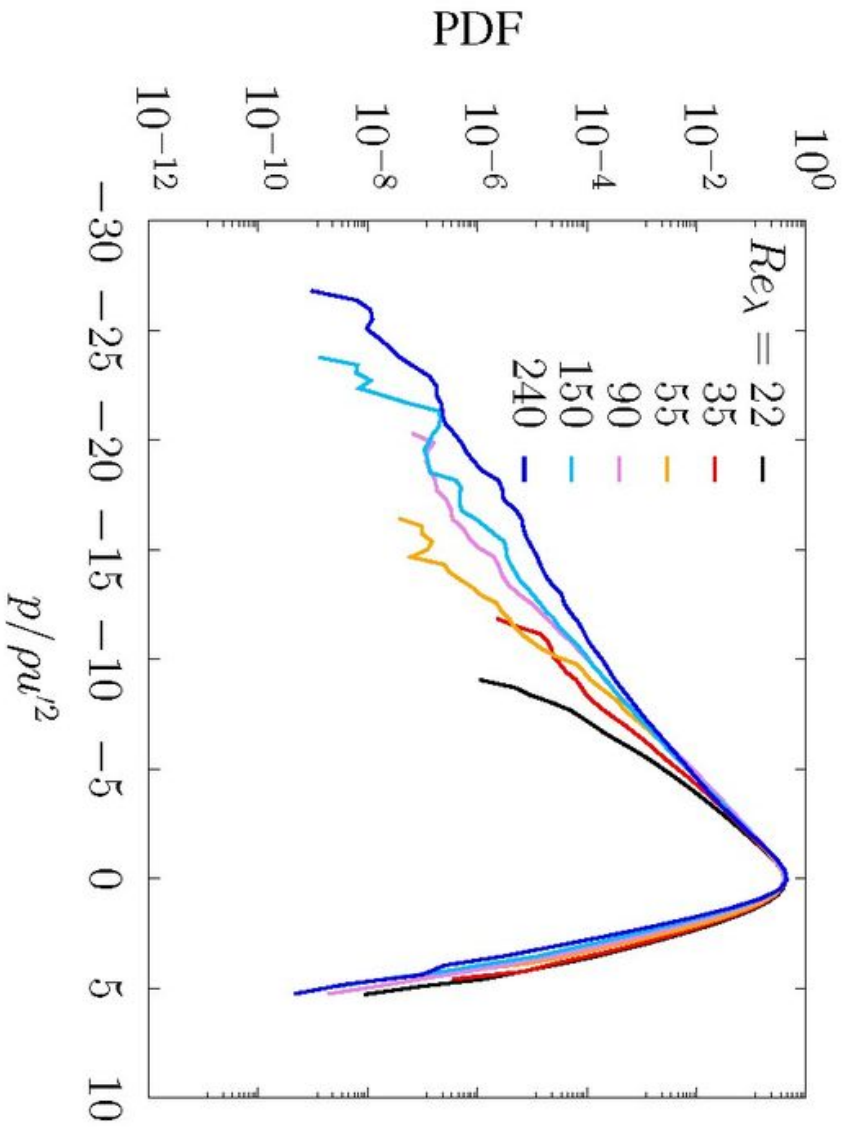

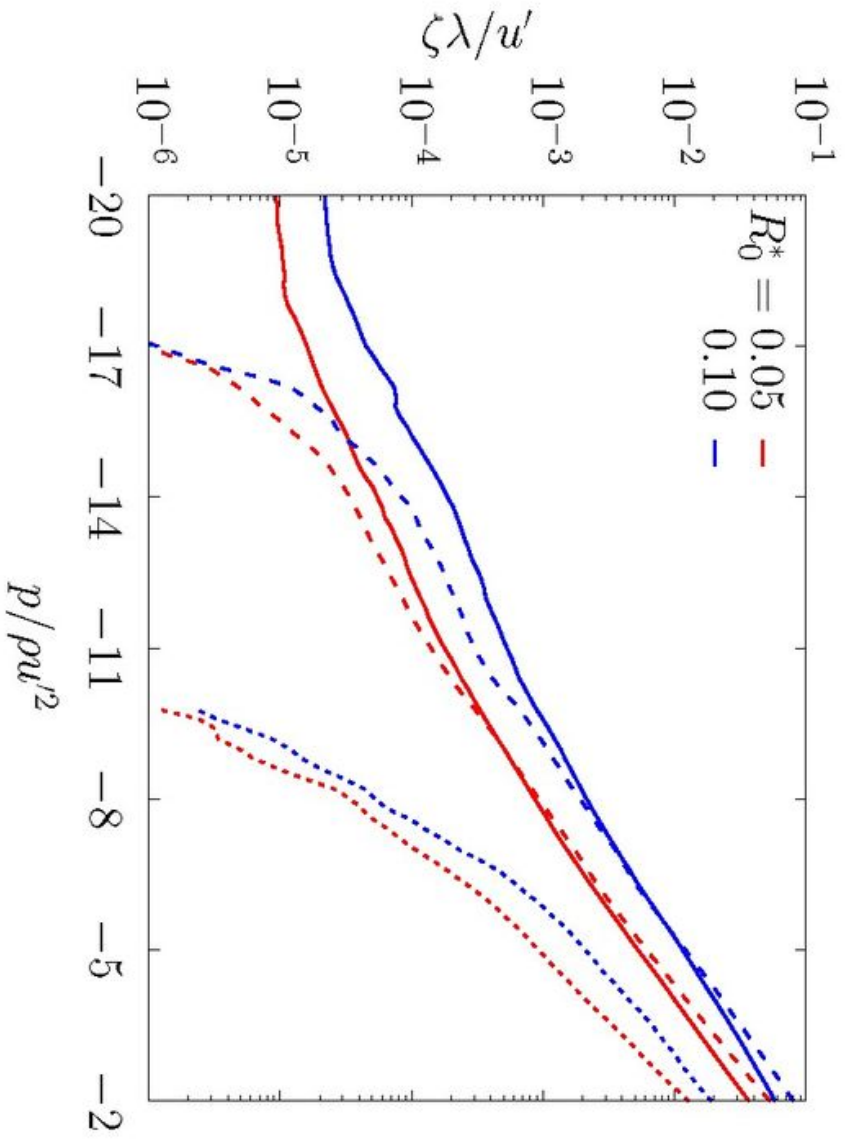

PLEASE CITE THIS ARTICLE AS DOI: 10.1063/5.0079313

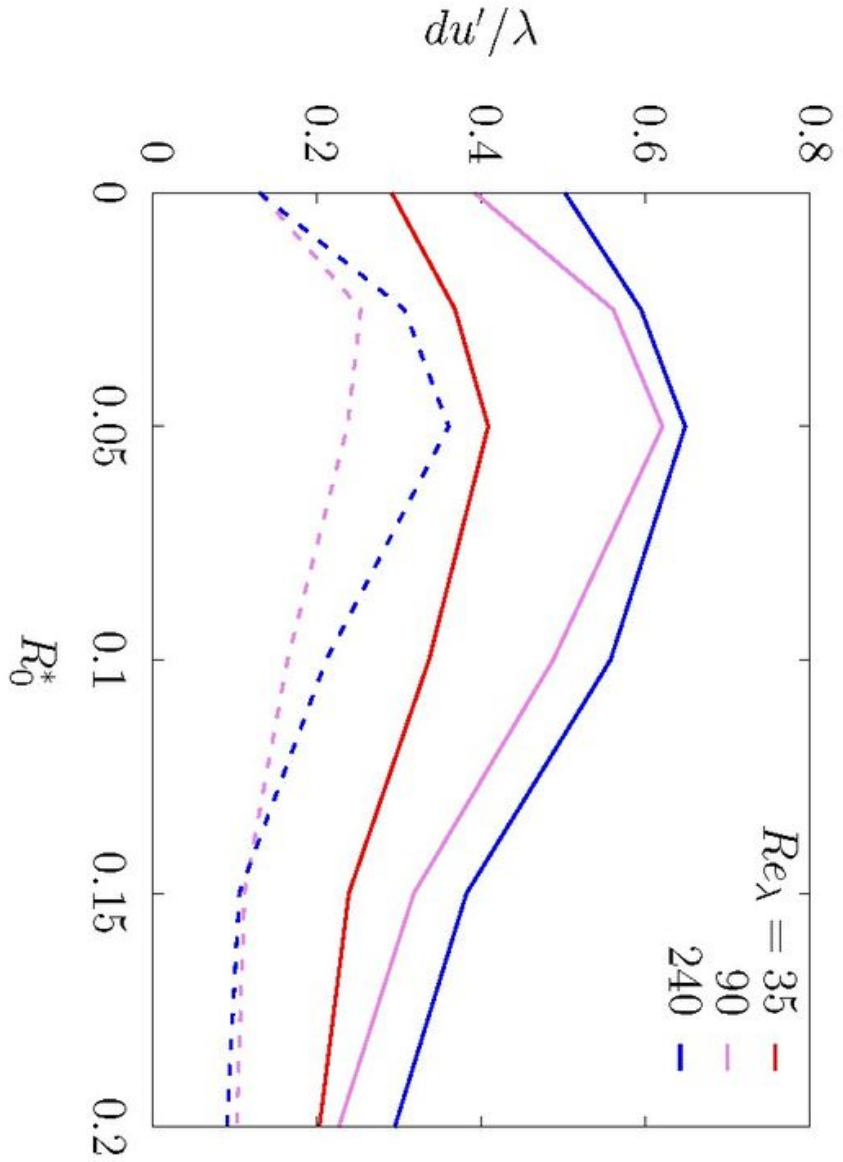

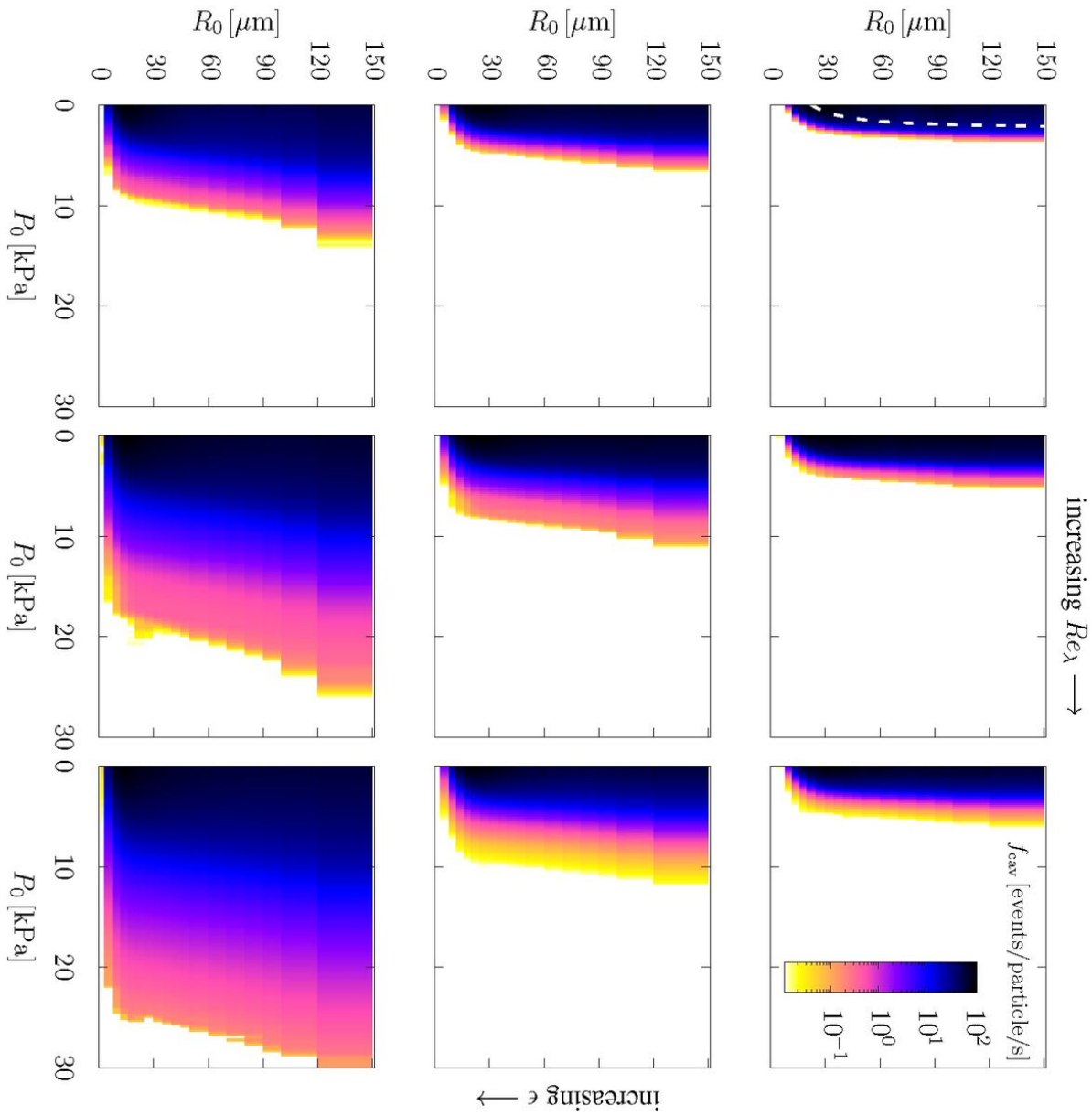

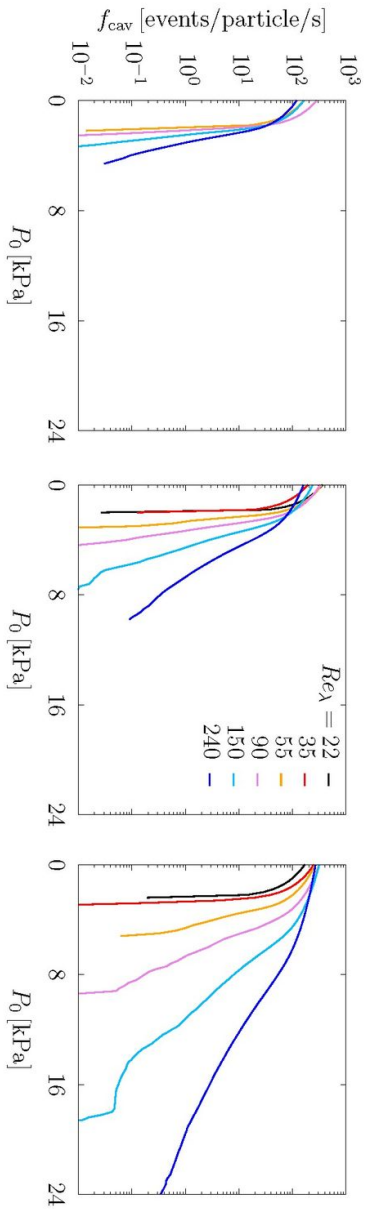

PLEASE CITE THIS ARTICLE AS DOI: 10.1063/5.0079313

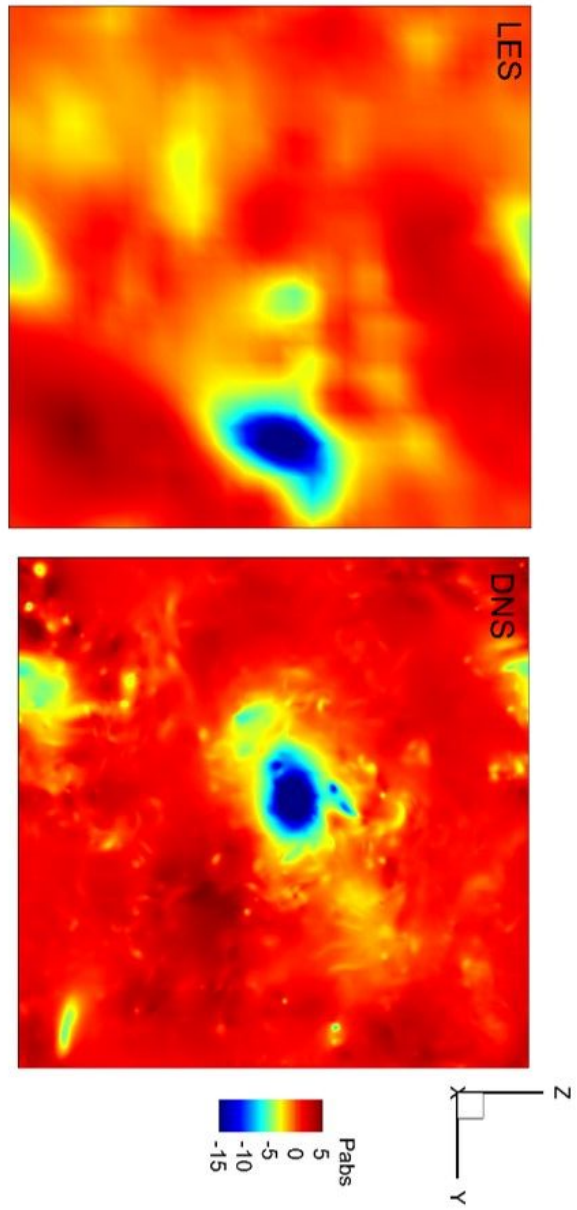

PLEASE CITE THIS ARTICLE AS DOI: 10.1063/5.0079313